Ab initio study of the migration of intrinsic defects in 3*C*-SiC

Michel Bockstedte,* Alexander Mattausch, and Oleg Pankratov
Lehrstuhl f. Theoretische Festkörperphysik, Universität Erlangen-Nürnberg, Staudtstrasse 7 B2, D-91058 Erlangen, Germany
(Received 12 March 2003; revised manuscript received 4 August 2003; published 3 November 2003)

The diffusion of intrinsic defects in 3*C*-SiC is studied using an *ab initio* method based on density functional theory. The vacancies are shown to migrate on their own sublattice. The carbon split-interstitials and the two relevant silicon interstitials, namely the tetrahedrally carbon-coordinated interstitial and the ⟨110⟩-oriented split interstitial, are found to be by far more mobile than the vacancies. The metastability of the silicon vacancy, which transforms into a vacancy-antisite complex in *p*-type and compensated material, kinetically suppresses its contribution to diffusion processes. The role of interstitials and vacancies in the self-diffusion is analyzed. Consequences for the dopant diffusion are qualitatively discussed. Our analysis emphasizes the relevance of mechanisms based on silicon and carbon interstitials.

DOI: 10.1103/PhysRevB.68.205201 PACS number(s): 61.72.Ji, 66.30.Lw, 66.30.Hs

I. INTRODUCTION

Silicon carbide is an important wide band-gap semiconductor which offers a variety of applications for high power and high frequency devices. During device processing, various intrinsic defects are introduced that affect the electronic properties of the material. The mobile intrinsic defects, namely vacancies and interstitials, play a pivotal role in self-diffusion and dopant diffusion as well as in the annealing of ion-implanted material.

Substitutional impurities are *per se* immobile. They need vacancies or interstitials as vehicles for the migration. The rapid diffusion in the course of annealing can considerably affect the implanted dopant profiles. For example, a transient enhanced dopant diffusion was observed in boron[1,2] and aluminum[3] implanted 4*H*-SiC. It is initiated by an excess concentration of intrinsic defects, most likely silicon interstitials as the analysis of recent experiments indicates[1,2,4,5] in contrast to the earlier assumption[6] of a vacancy-mediated mechanism. Similar mechanisms are operative in the more fundamental self-diffusion. As a matter of fact, a microscopic understanding of the mechanisms underlying the self-diffusion should provide insight into the mechanisms of the dopant diffusion. In the most recent studies[7–10] of self-diffusion in 3*C*- and 4*H*-SiC diffusion constants have been measured for the carbon and silicon self-diffusion. The basic diffusion mechanisms, however, have not been unraveled. In particular, the role of interstitials and vacancies in different diffusion processes remains open for both polytypes.

Alongside the diffusion, the annealing of mobile intrinsic defects contains information about the migration of vacancies and interstitials. The annealing of vacancy-related defects has been studied by positron annihilation spectroscopy[11–14] and electron-paramagnetic-resonance (EPR) techniques[15–18] in irradiated material. The identification of the EPR centers as isolated silicon[15,16] and carbon[18] vacancies has been verified theoretically.[16,19] It was found that the annealing behavior of carbon and silicon vacancies shows striking differences. For example, in EPR experiments[15] the silicon vacancy was found to anneal in several stages at 150 °C, 350 °C, and 750 °C, whereas for the carbon vacancy a single characteristic annealing temperature of 500 °C was observed.[18] Recently, an EPR center was observed by EPR experiments[20] in material annealed above 750°C and interpreted as a vacancy-antisite complex. This complex may be a decay product of the metastable silicon vacancy (in *p*-type and intrinsic material) as predicted by theory.[21,22] A comprehensive interpretation of annealing experiments in terms of elementary processes crucially depends on an understanding of the underlying diffusion mechanisms of intrinsic defects.

Theoretical investigations by *ab initio* methods can provide important insight in a microscopic picture of the self- and dopant diffusion as well as the annealing kinetics. In the present paper we investigate the mobile intrinsic defects and their migration mechanisms in 3*C*-SiC using a method based on density-functional theory. The Frenkel pair recombination and other diffusion-controlled annealing mechanisms are treated elsewhere.[23] Our investigation is based on recent theoretical studies of the ground-state properties of vacancies[24,25] and antisites[25] and addresses interstitials and vacancy-antisite complexes that are relevant for the migration. We show that different types of silicon interstitials, which have entirely different migration paths, are important in *p*-type and *n*-type material. The metastability of the silicon vacancy in *p*-type material is demonstrated to have strong implications for vacancy-assisted diffusion mechanisms. The considered diffusion processes are summarized in Fig. 1, which shows the most important migration channels for vacancies and interstitials in 3*C*-SiC. We find that interstitials are by far more mobile than vacancies and therefore play a prominent role in the diffusion. We also demonstrate that the diffusion mechanisms strongly depend on the charge state of the mobile defects.

The outline of the paper is as follows. Beginning with a description of the method in Sec. II we turn to the ground-state properties of interstitials, vacancies, and vacancy-antisite complexes in Secs. III and IV. The migration mechanisms of vacancies and interstitials are analyzed in Sec. V. The role of interstitials and vacancies in the self-diffusion and dopant diffusion is discussed in Sec. VI. A summary concludes the paper.

 ©2003 The American Physical Society

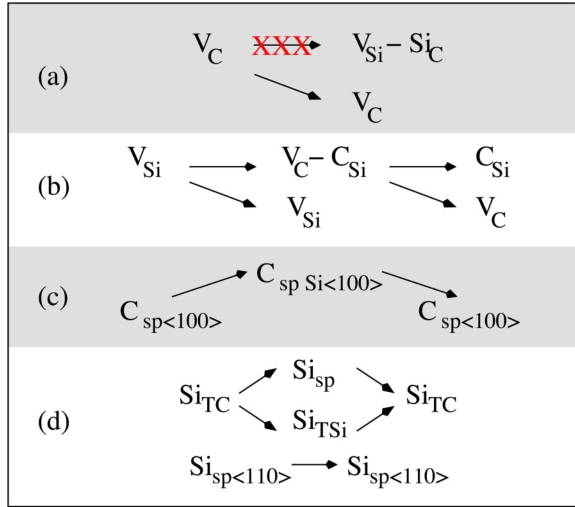

FIG. 1. The dominant migration mechanisms of interstitials and vacancies: (a) carbon vacancies (V_C) migrate on the carbon sublattice only, (b) transformation of the silicon vacancy (V_{Si}) into a carbon vacancy-antisite complex V_C-C_{Si} (p-type and compensated) and the vacancy migration on the silicon sublattice (n-type), (c) carbon-interstitial migration via split-interstitial configurations $C_{sp\langle 100\rangle}$ and $C_{spSi\langle 100\rangle}$, and (d) kick-out mechanism for the carbon-coordinated silicon interstitial (Si_{TC}) via split interstitials ($Si_{sp\langle 100\rangle}$ and $Si_{sp\langle 110\rangle}$) ($p$-type) and direct migration of the silicon split interstitial $Si_{sp\langle 110\rangle}$ (compensated and n-type material).

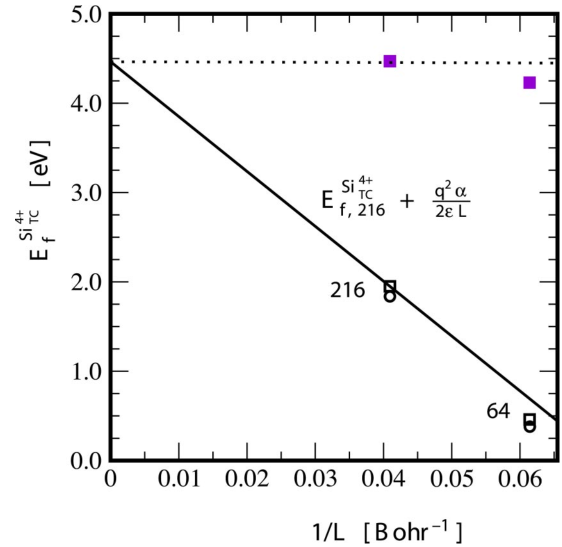

FIG. 2. Madelung corrections for the silicon interstitial Si_{TC}^{4+}. The formation energy $E_{Si,f}$ as calculated in the 64- and 216-atom cell with and without the Madelung correction (filled and open symbols, respectively) is plotted vs the inverse defect-defect distance. The squares and circles refer to a ($2\times2\times2$ mesh) k point set and the Γ point. The extrapolation of $E_f^{Si_{TC}}$ obtained in the 216-atom cell to the isolated defect using the monopole correction is shown by the solid line.

II. METHOD

We carried out first-principles calculations using the plane-wave pseudopotential package FHI96MD[26] within the framework of density-functional theory (DFT).[27,28] The local-density approximation[29] (LDA) is employed for the exchange-correlation functional and spin effects are included within the local spin-density approximation (LSDA) where necessary.

We describe the intrinsic defects and their environment using periodic supercells. Large supercells with 64 and 216 crystal lattice sites are used. The electron transitions between the defect and its periodic images give rise to the formation of defect bands and affect the defect energetics. This artificial defect-defect interaction can be efficiently reduced by a special k-point sampling.[30] A special k-point mesh[31] with eight k points in the Brillouin zone ($2\times2\times2$ mesh) provides converged defect energies for the 64-atom cell. It is crucial to preserve the correct degeneracy of the isolated defect levels, as the degeneracy may lead to a Jahn-Teller instability. In those cases, where symmetry-lowering Jahn-Teller distortions are important, we perform the calculations using only the Γ point in a 216-atom cell (for which already sufficiently converged formation energies are obtained), with the exact point symmetry of an isolated defect. In the case of charged defects we follow the approximate procedure of Makov and Payne[32] to account for the electrostatic interaction of the periodically arranged defects as well as their interaction with the compensating background. The relevance of such corrections has been already pointed out by Torpo *et al.* for the vacancies in $4H$-SiC.[25] Especially for the highly charged interstitial defects this procedure improves the defect energetics considerably. In Fig. 2 we demonstrate this for the carbon-coordinated silicon interstitial Si_{TC} (cf. Sec. III). We find that the completely ionized interstitial silicon (charge state 4^+) is strongly screened by the surrounding lattice. A comparison of the formation energies calculated for the 64- and 216-atom cell with and without the Madelung correction shows indeed that the correction leads to a more consistent description. Whereas we obtain 0.5 eV and 1.9 eV without the correction using special k points, the corrected results of 4.23 eV and 4.47 eV agree to within 0.24 eV. Here we have only included the dominant monopole correction ($q^2\alpha/2\varepsilon L$, where α is the Madelung constant of the simple cubic lattice, L is the defect-defect distance, and ε is the experimental dielectric constant); the quadrupole correction ($\sim qQ\varepsilon L^3$, where Q is the quadrupole moment) should lead to a smaller correction as suggested by the detailed analysis of Lento *et al.*[33]

Soft norm-conserving pseudopotentials of the Troullier-Martins type[34] and a plane-wave basis set are employed. The carbon pseudopotential has been optimized for calculations with a small basis set (matching radii $r_s^c = 1.6$ bohrs, $r_p^c = 1.7$ bohrs and $r_d^c = 1.5$ bohrs). For the silicon potential the standard parameters are used. With these pseudopotentials and a basis set including plane waves of a kinetic energy up to 30 Ry defect formation energies have been calculated with a basis set induced convergence error below 0.1 eV (for an energy cutoff of 40 Ry all energy differences are converged). For each defect the coordinates of all atoms in the supercell have been relaxed. This is essential to obtain a correct energetic description.

A. Formation energies

As a guide through the hierarchy of intrinsic defects one often uses their relative abundance in thermodynamic equilibrium. At constant volume the concentration of defects is determined by the free energy of defect formation F_{f}:

$$c_{\mathrm{D}}=c_{\mathrm{S}}\exp\left(-\frac{F_{\mathrm{f}}}{k_{\mathrm{B}}T}\right), \tag{1}$$

where c_{S} is the concentration of the sites that are open to the defect, k_{B} is the Boltzmann constant, and T is the temperature. The free energy of formation is specified by the formation energy E_{f} and the formation entropy S_{f} of the defect:

$$F_{\mathrm{f}}=E_{\mathrm{f}}-TS_{\mathrm{f}}. \tag{2}$$

Usually the defect abundance is well described by the formation energy E_{f} alone. Even though the formation entropy may amount up to 10 k_{B} [values of about 8 k_{B} have been recently reported for vacancies in Si (Ref. 35) and GaAs (Ref. 36)], its contribution can be relevant only at fairly high temperatures and for defects with comparable formation energies.

In the compound material SiC the equilibrium defect concentration depends on the chemical environment which is characterized by the carbon and silicon chemical potentials, μ_{C} and μ_{Si}. The chemical potentials may vary only within certain bounds to prevent the formation of other more stable phases than SiC. In excess of carbon (C-rich conditions) such a phase can be graphite. In the other extreme (Si-rich conditions), this would be crystalline silicon. The formation energy of a defect is calculated as[37,38]

$$E_{\mathrm{f}}=E_{\mathrm{D,\,cell}}-n_{\mathrm{C}}\mu_{\mathrm{C}}-n_{\mathrm{Si}}\mu_{\mathrm{Si}}-n_{\mathrm{e}}\mu_{\mathrm{F}}, \tag{3}$$

where $E_{\mathrm{D,\,cell}}$ is the total energy of the defect supercell, n_{C} and n_{Si} are the number of carbon and silicon atoms in the supercell. In case of an ionized defect, n_{e} is the number of excess electrons transferred from the Fermi level μ_{F} to the localized defect levels (for positively charged defects n_{e} is negative). In equilibrium, the chemical potentials of the environment μ_{C} and μ_{Si} are related to the chemical potential of the crystal μ_{SiC} by $\mu_{\mathrm{SiC}}=\mu_{\mathrm{C}}+\mu_{\mathrm{Si}}$. With this relation we eliminate μ_{C} in Eq. (3). We express the remaining free parameter $\mu_{\mathrm{Si}}=\mu_{\mathrm{Si}}^{0}+\Delta\mu$ in terms of the chemical potential of crystalline silicon μ_{Si}^{0} and the difference to this value $\Delta\mu$. These substitutions in Eq. (3) yield

$$E_{\mathrm{f}}^{n_{\mathrm{e}}}=E_{\mathrm{D}}^{n_{\mathrm{e}}}-(n_{\mathrm{Si}}-n_{\mathrm{C}})\Delta\mu-n_{\mathrm{e}}\mu_{\mathrm{F}}, \tag{4}$$

where $E_{\mathrm{D}}^{n_{\mathrm{e}}}=E_{\mathrm{D,\,cell}}^{n_{\mathrm{e}}}-n_{\mathrm{C}}\mu_{\mathrm{SiC}}-(n_{\mathrm{Si}}-n_{\mathrm{C}})\mu_{\mathrm{Si}}^{0}$ is expressed by the number of the involved atoms and chemical potentials, which are obtained by total-energy calculations for the perfect crystals. As described above, neither μ_{C} nor μ_{Si} can exceed the values of the corresponding bulk phases (graphite or diamond and silicon). Therefore $\Delta\mu$ may vary only between the negative heat of formation of the corresponding polytype $-H_{\mathrm{f,\,SiC}}$ and 0 (C-rich and Si-rich conditions, respectively). Our calculated value of the heat of formation amounts to 0.61 eV and depends only slightly on the polytype. This result is in good agreement with the value of 0.58 eV obtained by Zywietz *et al.*[24] and slightly lower than the experimental value of 0.72 eV. Here we have deliberately chosen diamond as the reference. This choice is comparable to the alternative choice of graphite due to the small energy difference between graphite and diamond. Note that our definition of the formation energy E_{D} is independent of this aspect. The value of E_{D} of Ref. 24 is retained by evaluating E_{f} for $\Delta\mu=-1/2\,H_{\mathrm{f,\,SiC}}$. For the calculation of charged defects it is convenient to state the value of the Fermi level μ_{F} relative to the valence-band edge E_{V}. In this case the energy E_{D} is given by the formula

$$E_{\mathrm{D}}^{n_{\mathrm{e}}}=E_{\mathrm{D,\,cell}}-n_{\mathrm{C}}\mu_{\mathrm{SiC}}-(n_{\mathrm{Si}}-n_{\mathrm{C}})\mu_{\mathrm{Si}}^{0}-n_{\mathrm{e}}E_{\mathrm{V}}. \tag{5}$$

The value of E_{V} is not reliably accessible in the calculation of the involved defects. Therefore we take the value E_{V} from a calculation for the perfect crystal and remove shifts in the average potential by aligning the bulk-spectrum features in the density of states of the defect cell and the defect-free cell. The alignment is consistent within 0.06 eV over the whole energy range. By this procedure we also verified that the defect cells contain a sufficiently large bulklike environment around the defect.

The realization of a specific charge state of a deep defect for a given Fermi level μ_{F} requires that the formation energy of the defect in the corresponding charge state is lower than for the other possible charge states and that all occupied single-particle levels lie below the conduction-band edge. Even though the Kohn-Sham levels have no physical interpretation by the design of the theory (only the electron density and the total energy are a well defined quantities), they reproduce the experimental quasiparticle band structure quite well. Yet, the calculated Kohn-Sham band gaps are usually smaller than experimental values (in 3*C*-SiC and 4*H*-SiC we obtain 1.2 eV and 2.2 eV as compared to the experimental findings of 2.39 eV and 3.27 eV). In this paper we follow a common practice (cf., e.g., Ref. 25) and use the experimental value for the conduction-band edge. With this approach it is not possible to unambiguously determine the charge states that are only stable in a region close to the conduction-band edge.

The thermodynamic ionization level of a charged defect is given by the value of the Fermi level at which the defect alters its charge state. It is obtained from the formation energy by

$$\varepsilon(q_2|q_1)=E_{\mathrm{D}}^{q_1}-E_{\mathrm{D}}^{q_2}. \tag{6}$$

Here q_1 and q_2 indicate the different charge states of the defect. Usually only one electron is transferred between the electron reservoir and the defect levels. A simultaneous transfer of two electrons is unfavorable due to the cost of the effective electron-electron repulsion. However, in some cases[39,40] the electron-electron repulsion can be compensated by a configurational relaxation arising from a strong electron-phonon coupling. This effect, known as the negative-*U* effect, leads to an attractive effective electron-electron interaction and the ionization level $\varepsilon(q-1|q)$ appears below $\varepsilon(q|q+1)$.

B. Defect migration

In order to analyze possible migration paths of interstitials and vacancies we apply two different standard methods. For the interstitial migration we use an implementation[41] of the ridge method of Ionova and Carter.[42] In this method, a saddle-point search is conducted for given initial and final configurations of the migration event, both configurations being slightly distorted towards each other. The two configurations are iterated such that they approach each other and the energy barrier along the line connecting the two configurations is minimized. By this procedure both configurations converge to the saddle point and the lowest migration energy barrier E_m is obtained. The search is repeated for all relevant charge states and the obtained transition states are analyzed. This automatic search of the saddle point fails when defect levels of different symmetry cross along the migration path. In this situation, which applies to the migration of vacancies, we analyze the potential-energy surface using the drag method. This approach has been previously employed in a study of the gallium vacancy migration in GaAs.[36] For a relevant set of coordinates (reaction coordinates), the potential-energy surface is calculated by constraining the coordinates of interest and minimizing the total energy for all remaining coordinates. The consistency of our choice of the reaction coordinates is verified. This includes the smoothness of the potential-energy surface as a function of the reaction coordinates. Details of the procedure are given in Sec. V, where the individual migration mechanisms are discussed.

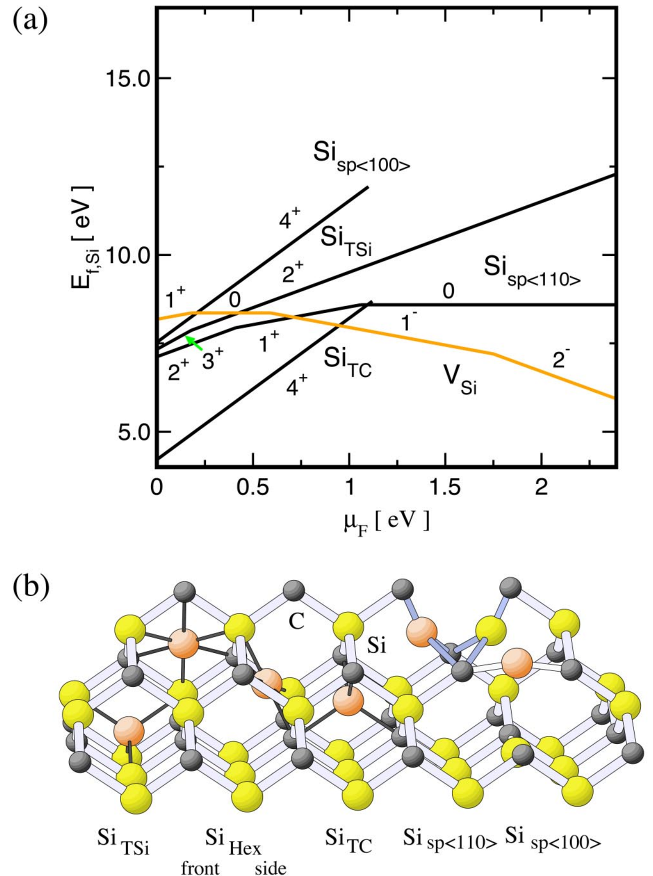

FIG. 3. Silicon interstitials: (a) formation energy for Si-rich conditions in comparison to the silicon vacancy (b) geometry of investigated interstitial sites; the hexagonal site is not stable.

III. INTERSTITIALS

A. Silicon interstitials

SiC as a compound semiconductor possesses various interstitial configurations, some of them being distinguished only by a carbonlike or siliconlike environment. Important interstitial configurations are depicted in Fig. 3. There are tetrahedral configurations with either four silicon or carbon neighbors and a hexagonal configuration. Besides these, split-interstitial configurations and bond-center configurations can exist. In a split configuration an interstitial silicon atom shares a site with a lattice atom, which could be either carbon or silicon. These dumbbell-like interstitials occur with orientations of the atom pair in the $\langle 100 \rangle$ and the $\langle 110 \rangle$ directions. In a bond-center configuration the interstitial silicon is centered at the bond of two neighboring lattice atoms.

We have considered all of the above configurations in our investigation. The hexagonal and bond-center interstitials as well as the split interstitials on the carbon sublattice turned out to be unstable in all relevant charge states. The calculated formation energies for the stable interstitials in comparison with the formation energy of the silicon vacancy (cf. Sec. IV) are displayed in Fig. 3 as functions of the Fermi level μ_F. To make the relation to Eq. (4) more transparent, we consider the case $\Delta\mu = 0$, i.e., Si-rich conditions, in Figs. 3 and 5. Since in case of silicon interstitials $n_{Si} - n_C = 1$, their formation energies rise by 0.61 eV when referring to C-rich conditions, while the formation energy of the silicon vacancy drops by the same amount. The charge states of the defects in the different ranges of μ_F are indicated. Except for the split interstitial $Si_{sp\langle 110 \rangle}$ all silicon interstitials are positively charged.

The hierarchy of silicon interstitials strongly depends on the position of the Fermi level. This is an immediate consequence of the existence of the deep interstitial levels. In p-type material the most abundant is the tetrahedrally carbon-coordinated interstitial Si_{TC} followed by the split interstitial $Si_{sp\langle 110 \rangle}$. Around midgap, this ordering changes: as the interstitial Si_{TC} is completely ionized (carrying a charge of 4^+) its formation energy rises more rapidly than that of the $Si_{sp\langle 110 \rangle}$ interstitial, which is neutral for μ_F around midgap. For Si_{TC} we can only estimate the formation energy of the charge states 3^+ (cf. below). This also applies for the split interstitial $Si_{sp\langle 100 \rangle}$. Therefore we have plotted the formation energy only up to the estimated position of the lowest ionization level. The tetrahedrally silicon-coordinated interstitial Si_{TSi} and the split interstitial with $\langle 100 \rangle$ orientation have a higher formation energy than the other stable configurations.

In the following we describe the electronic structure of silicon interstitials. The interstitial Si_{TC} does not introduce deep levels into the band gap. The silicon atom loses its valence electrons and becomes completely ionized. However, the interaction with the carbon and silicon neighbors induces an electron flow to the silicon interstitial, resulting in

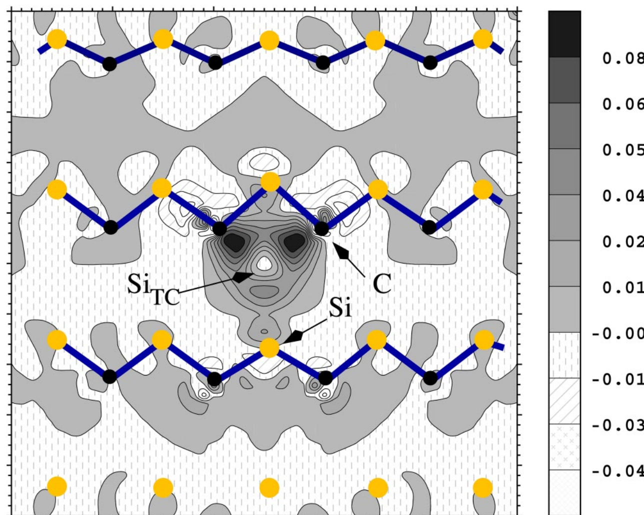

FIG. 4. Binding of $\mathrm{Si_{TC}}$: polarization $\delta n(\mathbf{r})$ of the electron density around the bare interstitial silicon ion at the $\mathrm{Si_{TC}}$ site obtained as a difference between the electron densities of the interstitial $n_{\mathrm{Si_{TC}}^{4+}}$ and of the bulk crystal n_{bulk} (calculated in the 216-atom cell).

an electron distribution that resembles that at a regular silicon lattice site. The *s* and *p* components of the electron density integrated over a sphere with a radius of 1.75 bohrs (half the nearest-neighbor distance in SiC) around the Si atom deviate from the values for a silicon site in a perfect crystal by less than 1%. This is also true for spheres of smaller radii. In Fig. 4 we have plotted the charge redistribution $\delta n = n_{\mathrm{Si_{TC}^{4+}}} - n_{\mathrm{bulk}}$, where $n_{\mathrm{Si_{TC}^{4+}}}$ is the electron density of the supercell containing the interstitial and n_{bulk} refers to the density of the perfect crystal. The polarization of the surrounding carbon-silicon bonds and the formation of bonds with the silicon interstitial is clearly visible. Although we have not found any localized one-particle levels within the band gap, we do not expect the charge state 4^+ to persist throughout the whole experimental band gap. Indeed, slightly above the experimental conduction-band energy we observe a localized state. Due to the large charge state correction the corresponding ionization level $\varepsilon(3^+|4^+)$ lies substantially lower, in a region somewhat above the experimental midgap. Thus the charge state 4^+ should be stable at least up to the midgap position of the Fermi level. Yet, the quantitative determination of the ionization level is not possible in DFT-LSDA calculations due to the well-known band-gap problem. The localized level is in resonance with the Kohn-Sham (and experimental) conduction band. To obtain their relative position (which is crucial for a correct occupation of levels) one would have to apply a *XC*-discontinuity correction to the conduction band and the localized state, which is well beyond the scope of the present work. This problem is less acute in 4*H*-SiC, where the band gap is substantially wider. We found[43] that the carbon-coordinated Si interstitial in 4*H*-SiC possesses a similar ionization level $\varepsilon(3^+|4^+)$ and a corresponding one-particle state that is located within the Kohn-Sham band gap.

TABLE I. Ionization levels of carbon and silicon interstitials with respect to the valence-band edge E_{V} in eV. The calculations have been performed in a 64-atom cell using special *k* points ($\mathrm{C_{sp\langle 100\rangle}}$ and $\mathrm{C_{spSi\langle 100\rangle}}$: 216-atom cell and Γ point to include spin polarization and Jahn-Teller distortions). Note that values for $\mathrm{C^0_{sp\langle 100\rangle}}$ and $\mathrm{C^-_{sp\langle 100\rangle}}$ correspond to the tilted configuration.

	$\mathrm{Si_{TSi}}$	$\mathrm{Si_{sp\langle 110\rangle}}$	$\mathrm{C_{sp\langle 100\rangle}}$	$\mathrm{C_{spSi\langle 100\rangle}}$	$\mathrm{C_{hex}}$	$\mathrm{C_{TSi}}$	$\mathrm{C_{TC}}$
$(2^+\|3^+)$	0.2						
$(1^+\|2^+)$		0.4	0.6	0.4	0.9	0.6	1.4
$(0\|1^+)$		1.1	0.8	0.7	1.3	1.1	1.8
$(1^-\|0)$			1.8	1.9	2.3	1.9	2.3
$(2^-\|1^-)$				2.3			

The screening of the silicon interstitial weakens the neighboring carbon-silicon bonds. This is manifested by an inward relaxation of the carbon neighbor shell towards the interstitial by 3.5% of an ideal bond length. The energy associated with this relaxation amounts to 4.82 eV. The relaxation of the first and- second-neighbor shells yields 4.37 eV, whereas the inclusion of only the first-neighbor shell results in a gain of 0.34 eV. This behavior shows the strong coupling between the induced polarization and the relaxation.

The tetrahedral interstitial $\mathrm{Si_{TSi}}$, in contrast to $\mathrm{Si_{TC}}$, has a deep nondegenerate level in the band gap below midgap. Its occupation enables charge states between 4^+ and 2^+. However, due to the charge state corrections, $\mathrm{Si_{TSi}^{4+}}$ is not realized. Only a single ionization level $(2^+|3^+)$ at 0.2 eV is present (cf. Table I). The state has *s*-like character at the interstitial silicon and *p*-like character at the fourth-neighbor carbon-atoms, which have a common bond with four silicon neighbors of $\mathrm{Si_{TSi}}$. There is only a negligible amplitude at the first-neighbor shell. The screened charge of the silicon ion induces a coupled rehybridization and relaxation: while the silicon neighbor shell relaxes outward (4.1 bohrs Si-$\mathrm{Si_{TSi}}$ distance), the carbon second-neighbor shell moves inward with a C-$\mathrm{Si_{TSi}}$ distance of 3.94 bohrs. Apparently, the unfavorable Si-Si bonds make this interstitial site less favorable than the $\mathrm{Si_{TC}}$ site. This explains also the observed instability of the hexagonal site, which would lie on the line connecting adjacent $\mathrm{Si_{TSi}}$ and $\mathrm{Si_{TC}}$ sites: The three fold carbon coordination cannot counterbalance the energy costs of the unfavorable silicon-silicon bond distance until the tetrahedrally carbon-coordinated site is reached.

In the split interstitials, as displayed in Fig. 3, the two silicon atoms that comprise the interstitial have a mutual distance of 4.1 bohrs ($\mathrm{Si_{sp\langle 110\rangle}}$) and 6.1 bohrs ($\mathrm{Si_{sp\langle 100\rangle}}$). The bonds of the $\mathrm{Si_{sp\langle 110\rangle}}$ interstitial are rearranged such that each of the silicon atoms has a threefold carbon coordination and a weak σ bond to its silicon partner. Within the band gap we find two nondegenerate deep levels below midgap (approximately at $E_{\mathrm{V}}+0.4$ eV and $E_{\mathrm{V}}+0.6$ eV) that possess antibonding character between the two silicon atoms. There is also a level close to the conduction band. Hence, one may expect that $\mathrm{Si_{sp\langle 110\rangle}}$ could exist in the charge states 4^+ to 2^-. However, according to our calculations only the charge states 2^+, 1^+, and neutral are realized. In the $\mathrm{Si_{sp\langle 100\rangle}}$ interstitial both silicon atoms are located in the interstitial 3.1 bohrs

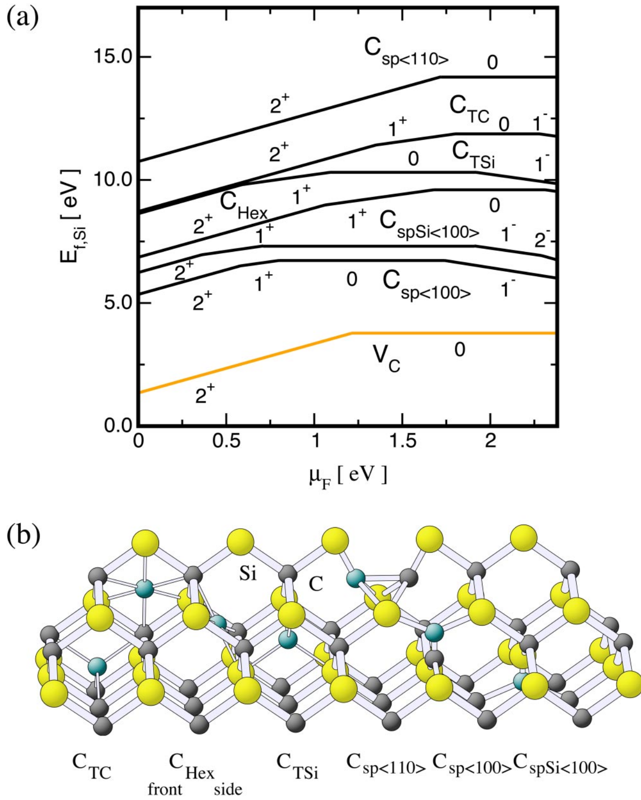

FIG. 5. Carbon interstitials: (a) formation energy for Si-rich conditions in comparison to the carbon vacancy (b) geometry of investigated interstitial sites.

away from the silicon lattice site. This structure corresponds to a complex of two Si_{TC} interstitials and a silicon vacancy. We do not find deep states in the band gap and the screening is almost prefect. According to our calculations this interstitial is almost unstable. However, it is an important intermediate configuration in the migration of the Si_{TC} interstitial.

B. Carbon interstitials

A different hierarchy is found for the carbon interstitials as for the silicon interstitials. In Fig. 5 we have depicted the stable carbon-interstitial configurations. The formation energies vs the Fermi level are displayed in Fig. 5(a) (for silicon rich conditions) in comparison with the formation energy of the carbon vacancy (cf. Sec. IV). In relation to Eq. (4) we again refer to Si-rich conditions. For C-rich conditions the formation energy of all carbon interstitials drops by 0.61 eV, whereas that of the vacancy rises correspondingly. The split interstitials with $\langle 100\rangle$-orientation ($C_{sp\langle 100\rangle}$ on the carbon sublattice and $C_{spSi\langle 100\rangle}$ on the silicon sublattice) have the lowest formation energy under all doping conditions. The hexagonal interstitial follows next in the hierarchy. The tetrahedral interstitials and the split interstitial with $\langle 110\rangle$ orientation are less favorable. For all interstitials deep levels exist in the band gap. The outlined hierarchy reflects the preference of carbon to form short bonds in the carbon split interstitial configurations $C_{sp\langle 100\rangle}$ and $C_{spSi\langle 100\rangle}$.

For $C_{sp\langle 100\rangle}$ we find two different configurations depending on the charge state, as illustrated in Fig. 6. In the positive

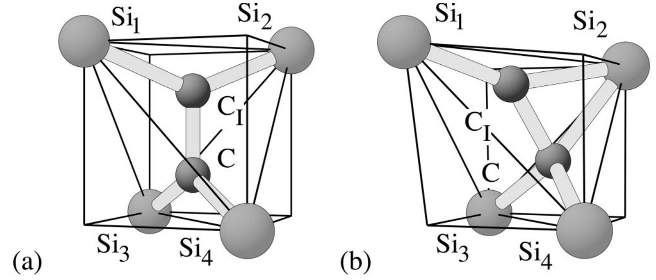

FIG. 6. Geometry of the carbon split interstitial $C_{sp\langle 100\rangle}$: (a) $\langle 100\rangle$ orientation with D_{2d}/D_2 symmetry, (b) tilted $C_{sp\langle 100\rangle}$. The $C_{spSi\langle 100\rangle}$ configuration corresponds to the untilted $C_{sp\langle 100\rangle}$ with the C-C_I pair replaced by a Si-C_I pair and C neighbors instead of Si-neighbors.

charge states the axis of the carbon pair is oriented along the $\langle 100\rangle$ direction. In the neutral and negative charge states this orientation becomes metastable. In the stable configuration the axis of the carbon pair is tilted in the corresponding $\{011\}$ plane. The new stable configuration arises from a pseudo-Jahn-Teller distortion of the untilted defect.

For $C^{2+}_{sp\langle 100\rangle}$ the carbon pair has a $\langle 100\rangle$ orientation. The symmetry of the defect is D_{2d}. We find a bond distance of 2.38 bohrs within the carbon pair and a silicon-carbon bond distance of 3.53 bohrs, which is close to the undistorted bond distance in SiC. Along the $\langle 100\rangle$-axis the original tetrahedral arrangement of the silicon neighbors is substantially distorted. The bond angle between the carbon-silicon bonds amounts to 137.5°. The electronic structure is dominated by the sp^2-like hybridization of the two carbon atoms. There is a twofold degenerate level (e representation) within the band gap. Besides four carbon-silicon σ bonds, the localized wave function contains an unhybridized p orbital at each carbon atom which is oriented perpendicular to the plane spanned by the σ bonds. In the case of $C^{+}_{sp\langle 100\rangle}$ the partial occupation of the degenerate state invokes a Jahn-Teller distortion. The distortion twists the defect molecule about its axis by 3.7° so that the silicon neighbors leave their original positions in the $\{011\}$ planes. This deformation lowers the energy as it allows a stronger interaction of the carbon p orbital with the silicon orbital. The symmetry becomes D_2. Besides the positively charged defect also the neutral and negative defects can be realized in this twisted configuration. However, in the neutral charge state the spin triplet is preferred over the singlet by 0.1 eV and the D_{2d}-symmetry is retained.

A tilting of the $\langle 100\rangle$ axis by 31° (in Fig. 6 in the plane Si_1-C_I-Si_2) transforms the metastable configuration of $C^{0}_{sp\langle 100\rangle}$ and $C^{-}_{sp\langle 100\rangle}$ into a stable configuration. Alongside the tilt a simultaneous shift of the atom pair occurs, such that the distance of the two carbon atoms to Si_2 becomes similar (C_I-Si_2: 3.7 bohrs and C-Si_2: 3.6 bohrs for $C^{0}_{sp\langle 100\rangle}$ and $C^{1-}_{sp\langle 100\rangle}$). While the distance within the pair (2.48 bohrs) only slightly increases, the distance Si_1-C_I is reduced to 3.2 bohrs. The distances Si_3-C and Si_4-C remain unaffected. The tilt and shift introduce a rehybridization of the bonds. Besides the carbon-carbon bond, the carbon atom C now binds to three silicon neighbors Si_2, Si_3 and Si_4, while C_I maintains bonds with only two silicon neighbors—a stronger one with

Si_1 and a weaker one with Si_2. The rebonding yields an energy gain of 0.6 eV. The metastable $\langle 100\rangle$-oriented configuration is separated from the tilted ground-state configuration by a low-energy barrier. In the neutral state the estimated energy barrier is only 0.06 eV.

The split interstitial $C_{spSi\langle 100\rangle}$ has a C_{2v} symmetry. Hence, for this interstitial only nondegenerate levels occur within the band gap, which have a similar sp^2 character as $C_{sp\langle 100\rangle}$. There are three levels around midgap. The lowest one has σ character. The two higher ones have a bonding character with the carbon neighbors and an admixed *p* character on the carbon atom. $C_{spSi\langle 100\rangle}$ occurs in the charge states 2^+ to 2^-, with the lowest electronic level being always completely occupied (cf. the ionization levels in Table I). The bond length of the atom pair is slightly shorter than the ideal SiC bond. This is also true for the bond between the silicon atom of the pair and its other carbon neighbors. The carbon-carbon bonds with a length of 2.8 bohrs are considerably shorter. Note that Jahn-Teller distortions are absent in this case. However, with the occupation of the non-degenerate defect levels the position of the silicon-carbon pair shifts along its axis.

The hexagonal interstitial C_{hex} as reflected by its C_{3v} symmetry has a nondegenerate level above midgap and a twofold degenerate level below the conduction band. The states originate from a localized *p* orbital that is oriented along the symmetry axis and from weak sp^2-like bonds with the carbon atoms of the hexagonal ring. In the relevant charge states 2^+, 1^+, and 0 only the nondegenerate *p*-like level is occupied. As a result the interstitial carbon is shifted along the hexagonal axis out of the center of the ring towards the carbon neighbors (bond distance 3.04 bohrs as compared to the distance to the silicon neighbors of 3.7 bohrs). In the charge state 1^- the occupation of the degenerate level leads to Jahn-Teller distortion, that lifts the axial symmetry. As a result, the interstitial carbon approaches two of the carbon neighbors.

A similar behavior is observed for the tetrahedrally carbon-coordinated configuration (C_{TC}), which has a nondegenerate and a threefold degenerate level within the band gap. Yet, the threefold coordinated configuration is energetically preferred over the tetrahedral configuration, since in the latter case the optimization of the carbon-carbon bonds results in an unfavorable elongation of surrounding carbon-silicon bonds. At the silicon-coordinated site favorable carbon-carbon bonds are not available. Therefore these configurations as well as the $\langle 110\rangle$-oriented split configuration are scarcely occupied in the thermodynamic equilibrium.

IV. VACANCIES AND VACANCY-ANTISITE COMPLEXES

A. Vacancies

The properties of the carbon and silicon vacancies (V_C and V_{Si}) in 3*C*- and 4*H*-SiC have been discussed in detail in the literature.[16,24,25,44–47] We summarize these results as necessary ingredients for the following discussion of the vacancy-antisite complexes and the mechanisms of the vacancy migration.

In Figs. 3 and 5 our results for the formation energy of V_{Si} and V_C are compared to the formation energy of the corresponding interstitials for Si-rich conditions. V_C is by far more abundant than carbon and silicon interstitials. This dominance also prevails in stoichiometric and C-rich material. V_{Si}, on the other hand, is less abundant than the interstitials in *p*-type material and dominates under intrinsic and *n*-type conditions. Furthermore, it has a higher formation energy than carbon vacancies. Hence, the equilibrium concentration of silicon vacancies is by several orders of magnitude lower.

The electronic structure of both unrelaxed vacancies derives from the four dangling bonds of the nearest neighbors. They have T_d symmetry and possess a threefold degenerate one-electron level (t_2 representation) within the band gap. The corresponding nondegenerate a_1 level falls below the valence-band edge. The occupation of the degenerate t_2-level either induces a Jahn-Teller distortion or leads to the formation of a nondegenerate high-spin state. The particular distinction between V_C and V_{Si} is the extended character of the silicon dangling bonds of the former vs the strong localization of carbon dangling bonds of the latter.[24] Driven by the overlap between the silicon dangling bonds, a considerable Jahn-Teller distortion of V_C is observed.[24,25] For V_{Si}, in contrast, correlation effects are more important[16,44,45] than the electron-phonon coupling. As a consequence, a multiplet state is formed[45,47] which leads to the preference for a high-spin state,[16,48] as predicted by DFT calculations[24,48] for all charge states.

In Table II we have summarized the ionization levels of the two vacancies in 3*C*- and 4*H*-SiC for the cubic and hexagonal sites. In the following we judge the realization of the different charge state using the experimental band gap as noted in Sec. II. According to our findings, V_{Si} exists in the charge states 1^+ through 2^- in 3*C*-SiC. In 4*H*-SiC also the charge states 3^- and 4^- are possible. V_{Si}^{2+} is not realized as a ground state with the inclusion of charge state corrections, a finding[49] that is verified by Ref. 25. Our ionization levels are in good agreement with the results of Ref. 25 obtained including charge state corrections. A slight deviation from the results of Zywietz *et al.*[24] originates from their neglect of these corrections and a different definition of the reference for the negative charge states. The realization of the charge states 3^- and 4^- is also observed in DFT-LSDA calculation in 6H-SiC (Ref. 20) using the (linear muffin-tin orbital-atomic sphere approximation) LMTO-ASA Green's function approach as well as the charge state 2^+. In comparison with our results in 4*H*-SiC, the calculated ionization levels agree to within 0.3 eV including the levels $\varepsilon(3^-|2^-)$ and $\varepsilon(4^-|3^-)$. We consider this as a good agreement taking the variation of the levels among the different polytypes and the inequivalent lattice sites into account (it was not stated in Ref. 20 to which site the calculations referred).

The carbon vacancy exists only in the charge states 2^+ and neutral in 3*C*-SiC. An enhanced electron-phonon coupling found for V_C^0 and V_C^{2-} destabilizes the charge states 1^+ and 1^-. The negative-*U* amounts to 0.15 eV (V_C^+). However, as the recent identification of V_C^+ by a comparison of the experimental hyperfine tensors and the calculated hyperfine interaction in 4*H*-SiC (Ref. 19) indicates, the prediction

TABLE II. Ionization levels of the native vacancies and the carbon vacancy-antisite complex in 3C- and 4H-SiC (cubic and hexagonal sites are denoted as k and h, respectively). The results have been obtained using a 216-atom cell (3C) and a 128-atom cell including spin polarization for the silicon vacancy.

		$(+\|2^+)$	$(0\|+)$	$(-\|0)$	$(2^-\|-)$	$(3^-\|2^-)$	$(4^-\|3^-)$
V_C	3C	1.29	1.14	2.69	2.04		
V_C	4H,k	1.29	1.17	2.23	2.11		
V_C	4H,h	1.05	0.97	2.23	2.05		
V_{Si}	3C		0.18	0.61	1.76		
	4H,k		0.21	0.70	1.76	2.34	2.79
	4H,h		0.30	0.76	1.71	2.42	2.90
V_C-C_{Si}	3C	1.24	1.79	2.19			
V_C-C_{Si}	4H,k	0.91	1.51	1.87	2.34	3.3	
V_C-C_{Si}	4H,h	0.83	1.39	2.11	2.56	3.12	

of the small negative-U maybe artificial. In 4H-SiC also the charge states 1^- and 2^- can be realized apart from the negative-U effect found for V_C^-. Note that the ionization levels of V_C vary between the cubic and hexagonal sites. This stems from the different arrangement of the third-nearest neighbors and translates into a different hybridization of the defect levels.

B. Vacancy-antisite complexes and the metastability of V_{Si}

For the migration two vacancy-antisite complexes are important: V_{Si}-Si_C and V_C-C_{Si}, where the antisite is the nearest neighbor of the vacancy. These complexes are obtained from V_C and V_{Si}, by a displacement of a silicon/carbon neighbor into the empty lattice site as illustrated in Fig. 7.

We have found that the V_{Si}-Si_C complex does not possess a stable configuration in all relevant charge states. As a result it decays into the carbon vacancy. The origin is a size effect: both, the silicon antisite and the silicon vacancy, show a strong outward relaxation.[48] For the antisite this relaxation optimizes the silicon-silicon bond distance to its neighbors, yet the bond remains strained as the ideal value of silicon bulk cannot be achieved. In the vacancy-antisite complex the missing silicon neighbor gives room for further relaxation by moving the antisite towards the vacancy. Additionally, the energy of the dangling bond located at the antisite is reduced by interacting with the carbon neighbors of the vacancy. As a result the barrier towards the vacant site vanishes. The unstable vacancy-antisite complex transforms into a stable carbon vacancy. From the above arguments we expect that our result for 3C-SiC (Ref. 22) is also valid in other polytypes. This expectation is supported by a DFT-based tight-binding calculation for the neutral complex in 4H-SiC.[21]

In contrast to V_{Si}-Si_C the carbon vacancy-antisite complex V_C-C_{Si} is stable. In fact, it is even more stable than the silicon vacancy in p-type material and for a Fermi level in a midgap range. This is shown in Fig. 8. Before we discuss the details and consequences of this metastability of the silicon vacancy, we briefly turn to the electronic structure of the complex.

Similar to the vacancies its localized levels within the band gap derive from the four dangling bonds at the carbon antisite and the silicon neighbors of the vacancy. By the C_{3v} symmetry of the ideal defect these dangling bonds give rise to two nondegenerate a levels and a doubly degenerate e level. As for the vacancies one a level forms a resonance in the valence band. The other a level lies at $E_V+1.8$ eV and the e level is found at $E_V+2.1$ eV $[(V_C\text{-}C_{Si})^+]$. Whereas the character of the localized a levels is dominated by the carbon dangling bond at the antisite, the e level derives from the three silicon dangling bonds. In the charge states 2^+, 1^+, and 0 the a level is occupied. The occupation of the e level for $(V_C\text{-}C_{Si})^-$ gives rise to a Jahn-Teller effect, which lowers the symmetry to C_{1h}. According to our findings, the charge state $(V_C\text{-}C_{Si})^{2-}$ is unstable (cf. Table II). In 4H-SiC the carbon vacancy-antisite complex shows similar properties. For our present purpose it is sufficient to treat the complexes aligned along the hexagonal axis. In this case the vacancy and the antisite occupy either neighboring hexagonal or cubic sites. The larger band gap of 4H-SiC (3.3 eV as compared to 2.4 eV in 3C-SiC) enables the negative charge states 2^- and 3^-.

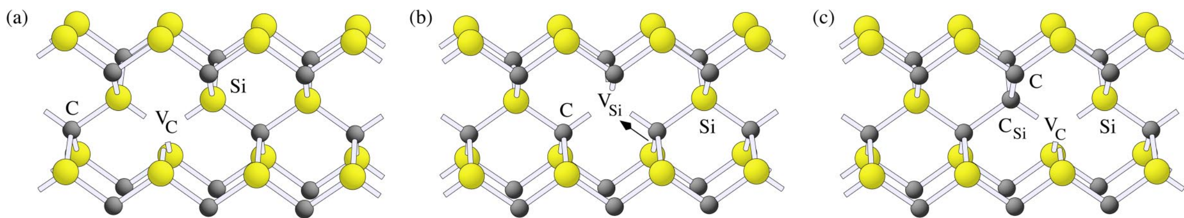

FIG. 7. Geometry of (a) the carbon vacancy V_C, (b) the silicon vacancy V_{Si}, and (c) the carbon vacancy-antisite complex V_C-C_{Si}. The hop of a carbon neighbor that transforms the silicon vacancy into a carbon vacancy-antisite complex is indicated by an arrow in (b).

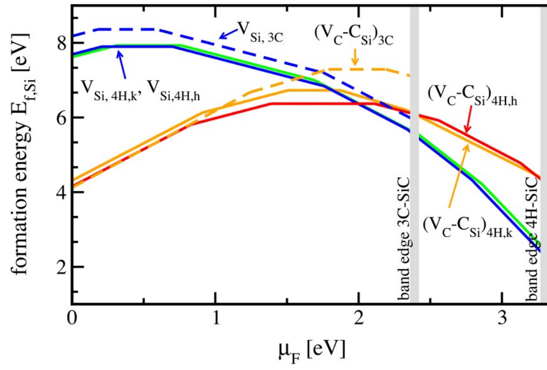

FIG. 8. Formation energy of the silicon vacancy V_{Si} and the carbon vacancy-antisite complex V_{C}-C_{Si} for 3*C*-SiC and 4*H*-SiC. The experimental band edges of 3*C*- and 4*H*-SiC are indicated by vertical bars.

The metastability of V_{Si} and its stabilization in *n*-type material occurs in both 3*C*- and 4*H*-SiC. As Fig. 8 shows, V_{C}-C_{Si} is more stable than V_{Si} under *p*-type conditions and for a midgap Fermi level. Its transformation into V_{C}-C_{Si} is associated with a large energy gain (about 4 eV for a Fermi level at the valence band). Since the defect levels of the V_{C}-C_{Si} complex are located above the levels of V_{Si}, the energy gain is reduced by the successive occupation of defect levels. This leads to a stabilization of V_{Si} over V_{C}-C_{Si} for *n*-type conditions. Only a metastability was observed[49] using special *k* points in a 64-atom cell. In this case, the formation energy of the silicon vacancy is higher in the negative charge states than the value we obtain in the 216-atom cell. The silicon vacancy and the vacancy-antisite complex have similar formation energies for a Fermi level above mid-gap in 4*H*-SiC, for the cubic complex at $\mu_{\mathrm{F}}=1.8$ eV and for the hexagonal complex at $\mu_{\mathrm{F}}=2.0$ eV. In 3*C*-SiC the formation energies match at $\mu_{\mathrm{F}}=1.8$ eV. The strong interaction between the vacancy and the antisite is reflected in the binding energy of the complexes. The binding energy ranges between 1.2 eV (2^+) and 1.0 eV (1^-).

Using a LMTO-ASA Green's-function approach based on DFT and LSDA, Lingner *et al.*[20] obtain similar results for 6*H*-SiC. A metastability of the silicon vacancy is also predicted by their calculations. The Fermi level at which the V_{Si} and the complex have similar energies is located above 2.8 eV. However, in their calculations the metastability is more pronounced which leads to a larger energy gain of the transformation. According to Fig. 7 of Ref. 20 the energy difference amounts to 4 eV (2.6 eV for the unrelaxed defects) for the neutral defects. Using DFT-based tight-binding calculations the authors obtain 1.6 eV. Our calculations yield 1.1 eV for 3*C*-SiC, 1.1 and 1.3 eV for cubic and hexagonal defects in 4*H*-SiC, which is much closer to the tight-binding result. For the carbon vacancy-antisite complex they obtain similar ionization levels for the positive and neutral charge states of the unrelaxed complex. Including relaxations a negative-*U* effect is found that is not observed in our calculations. Yet, as noted above the agreement of the ionization levels of the silicon vacancy is good. It indicates that the formation energy of the silicon vacancy is essentially shifted by about 3 eV (1.3 eV for the unrelaxed defects) with respect to the value of the carbon vacancy-antisite complex as compared to our calculations. Consequently, the Fermi level at which the silicon vacancy and the complex have a comparable formation energy is found closer to the conduction-band edge as in our case.

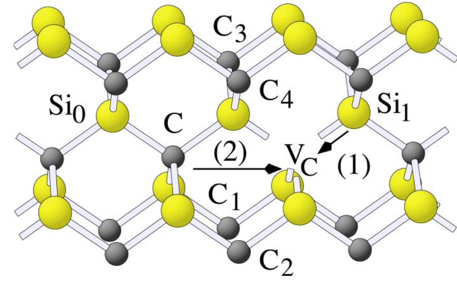

FIG. 9. Migration of the carbon vacancy V_{C}: (1) initial nearest-neighbor hop, (2) migration on the carbon sublattice by second-neighbor hops.

V. MIGRATION

A. Carbon vacancies

For the migration of the vacancies we have analyzed two mechanisms that involve either nearest-neighbor hops as observed in silicon[35] or second-neighbor hops, which are, e.g., relevant for the gallium vacancy in GaAs.[36,50,51] The two hops are depicted in Fig. 9. As discussed in Sec. IV, nearest-neighbor hops transform the vacancy into a vacancy-antisite complex. In successive hops the vacancy would proceed leaving behind a chain of antisites, which is energetically unfavorable. In the ring mechanism proposed by Van Vechten[52] this is avoided by the vacancy passing twice through the same sixfold ring. We have shown in Sec. IV that the silicon vacancy-antisite complex is unstable. For the carbon vacancy, this finding rules out any migration mechanism based on nearest-neighbor hops.

In our analysis of the migration by second-neighbor hops and the calculation of the migration barriers, we follow the procedure in Ref. 36. There it was shown for the gallium vacancy in GaAs that the migration mechanism involves the motion of the hopping gallium atom (a C atom in Fig. 9) and its common neighbor with the vacancy (the Si neighbor in Fig. 9). At the saddle point, the hopping atom passes through the plane spanned by the four atoms ($C_1, \ldots, C_4$ in Fig. 9) that we refer to as the gate below. In order to accommodate the strain of this configuration it is favorable for the nearest neighbor to relax towards either of the vacant lattice sites. Thus two saddle points and correspondingly two migration paths exist for the hop—one, where the neighbor of the vacancy passes through the gate prior to the second neighbor and one where the latter passes first. Following Ref. 36, we introduce two reaction coordinates ξ_{C} and ξ_{Si} for the hopping carbon atom and the common silicon neighbor by

$$\xi_{\mathrm{C/Si}}=\left(\mathbf{R}_{\mathrm{C/Si}}-\frac{1}{4}\sum_{i=1}^{4}\mathbf{R}_{C_i}\right)\cdot\mathbf{e}_{110}, \tag{7}$$

TABLE III. Vacancy migration: the migration barrier and geometry at the transition state for the migration by second-neighbor hops and the transformation of $V_{\rm Si}$ into $V_{\rm C}$-$C_{\rm Si}$ (initial nearest-neighbor hop). See the text for details.

		2^+	1^+	0	1^-	2^-
$V_{\rm C}\rightarrow V_{\rm C}$	$E_{\rm m}$ (eV)	5.2	4.1	3.5		
	$\xi_{\rm Si}$ (bohrs)	0.82	0.79	0.78		
	Si-Si$_0$ (bohrs)	4.80	4.79	4.76		
	Si-Si$_1$ (bohrs)	7.07	6.79	6.57		
$V_{\rm Si}\rightarrow V_{\rm Si}$	$E_{\rm m}$ (eV)		3.6	3.4	3.2	2.4
	$\xi_{\rm C}$ (bohrs)		0.57	0.30	0.01	0.03
	C-C$_0$ (bohrs)		5.08	5.56	5.93	5.97
	C-C$_1$ (bohrs)		6.74	6.33	5.96	6.00
$V_{\rm Si}\rightarrow V_{\rm C}$-$C_{\rm Si}$	$E_{\rm m}$ (eV)		1.9	2.4 (2.2)	2.5	2.7
$V_{\rm C}$-$C_{\rm Si}\rightarrow V_{\rm Si}$	$E_{\rm m}$ (eV)	6.1	4.2	3.5	2.4	
	$\Delta\xi_{\rm NN}$ (bohrs)	1.96	1.53	1.64 (1.97)	1.67	1.67
	$\xi_{{\rm NN},\perp}$ (bohrs)	0.00	0.05	0.19 (−0.11)	0.12	0.28

where $\mathbf{R}_{\rm C/Si}$ for $\xi_{\rm C}$ and $\xi_{\rm Si}$, respectively, refers to the coordinates of the carbon or silicon atom and the $\mathbf{R}_{{\rm C}_i}$ are the coordinates of the four carbon atoms comprising the gate; $\mathbf{e}_{110}$ is the unit vector of the direction connecting the initial and final lattice sites of the vacancy [here the (110) direction is chosen]. Instead of evaluating the full potential-energy surface for these two coordinates, we consider only the region in the vicinity of the transition state. For a given $\xi_{\rm C}$ the total energy is minimized with respect to $\xi_{\rm Si}$ and the other atomic coordinates. We find indeed the behavior we have discussed above. The transition state lies by 0.2 eV lower than the configuration where the carbon atom and its silicon neighbor pass through the gate at the same time. The barriers are obtained using the 216-atom cell together with the Γ point, which also allowed for the proper inclusion of Jahn-Teller distortions in the initial configurations. The results for the migration barrier and the geometry at the transition state are given in Table III. Using a 64-atom cell and special k points ($2\times2\times2$ Monkhorst-Pack mesh), the calculated barriers agree to within 0.3 eV. We find relatively high migration barriers between 5 eV ($V_{\rm C}^{2+}$), 4.1 eV ($V_{\rm C}^{+}$), and 3.5 eV ($V_{\rm C}^{0}$). The migration barrier in n-type material and with a Fermi level around midgap ($V_{\rm C}^{0}$) is much smaller than in p-type material ($V_{\rm C}^{2+}$). This stems from the different occupation of bonding defect levels at the transition state. Besides the bond between the common Si neighbor and Si$_0$ (cf. Fig. 9), the remaining three dangling bonds at the opposite vacant site contribute to the defect levels in the band gap. With the occupation of the lowest level the corresponding neighbor (Si$_1$) relaxes towards the vacant site, thus reducing the distance to the silicon neighbor and the migration barrier.

B. Silicon vacancies

In case of the silicon vacancy the migration by second-neighbor hops competes with the transformation $V_{\rm Si}\leftrightarrow V_{\rm C}$-$C_{\rm Si}$. Particularly in p-type material, the metastability of the silicon vacancy will have consequences for its migration. However, a migration of the silicon vacancy solely based on nearest-neighbor hops is impossible. This is due to our finding that the second configuration in such a mechanism, the $V_{\rm Si}$-Si$_{\rm C}$-C$_{\rm Si}$ complex, is unstable in all relevant charge states. In order to understand the consequences of the metastability, the barriers for the second-neighbor hop and the transformation $V_{\rm Si}\leftrightarrow V_{\rm C}$-$C_{\rm Si}$ have to be compared.

The analysis of the second-neighbor hop proceeds as detailed in the preceding section. This mechanism has essentially the same features as in the case of the carbon vacancy. Now the second silicon neighbor and the nearest carbon neighbor take the role of the respective carbon and silicon atom in the discussion of $V_{\rm C}$. The calculations have been performed within the 216-atom cell using the Γ point and including spin polarization. For the 64-atom cell and a special k-point sampling we obtain within 0.2 eV the same barriers. Our results for the barriers and the geometry at the transition state are listed in Table III. At the transition state the displacement of the carbon neighbor out of the gate is less pronounced as in the case of the carbon vacancy. For the negative vacancy it almost vanishes. We explain this by the rather small extent of the carbon orbitals and the resulting weak interaction of the carbon neighbor with the other carbon dangling bonds. The migration barrier for this mechanism varies between 3.6 eV ($V_{\rm Si}^{+}$) and 2.4 eV ($V_{\rm Si}^{2-}$).

Our analysis of the nearest-neighbor (NN) hop parallels the approach to the second-neighbor hop. We introduce the reaction coordinate $\xi_{\rm NN}$ which measures the distance of the hopping carbon atom from the center of mass of its three silicon neighbors. It is given by

$$\xi_{\rm NN}=\left(\mathbf{R}_{\rm C}-\frac{1}{3}\sum_{i=1}^{3}\mathbf{R}_{{\rm Si}_i}\right)\cdot\mathbf{e}_{111},$$

where $\mathbf{R}_{\rm C}$ is the coordinate of the hopping carbon atom and $\mathbf{R}_{{\rm Si}_i}$ are the coordinates of its three silicon neighbors; $\mathbf{e}_{111}$ is the unit vector in the direction of the hop [here chosen as the (111) direction]. Note that this approach allows for a migration path that deviates from the (111) direction.

As detailed in Sec. IV, V_{Si} and V_C-C_{Si} are found in different charge states for a given Fermi level. We assume that the charge state of the defect is preserved during the transformation. The necessary electron transfer to obtain the equilibrium charge state occurs in the final configuration. Harrison has shown[53] for the case of the interstitial in silicon that this assumption is reasonable. This applies also to the transformation of $V_{Si}^{2-} \rightarrow (V_C\text{-}C_{Si})^{2-}$ and $(V_C\text{-}C_{Si})^{2+} \rightarrow V_{Si}^{2+}$, where the final configurations $(V_C\text{-}C_{Si})^-$ and V_{Si}^+ are the ground-state configurations.

The energy barriers and the values of the reaction coordinate ξ_{NN} at the transition state are listed in Table III. The barrier for the transformation $V_{Si} \rightarrow V_C$-C_{Si} moderately depends on the charge state. It is by 0.8 eV lower for the positive vacancy than for the doubly negative charge state. The reverse transformation V_C-$C_{Si} \rightarrow V_{Si}$ shows a much stronger charge state dependence. A barrier of 6.1 eV is found for $(V_C\text{-}C_{Si})^{2+}$, which lowers down to 2.4 eV for $(V_C\text{-}C_{Si})^-$. During the transformation the hopping carbon atom moves away from the (111) direction. In this way it optimizes the number of bonds maintained with its silicon and carbon neighbors. A path along the (111) direction has a much larger energy barrier, due to a simultaneous breaking of three bonds with the silicon neighbors. Only this latter path was obtained[49] using the 64 atom cell with a special k point sampling and was reproduced using the 216 atom cell. However, this path is not important.

For all charge states the transformation $V_{Si} \rightarrow V_C$-C_{Si} mainly occurs in a low-spin state of the vacancy. Typically much higher barriers are found for the high-spin state, except for V_{Si}^0 where the high-spin state has a slightly lower barrier (given in braces in Table III). Note that the ground state of the vacancy-antisite complex is always a low-spin state for all charge states. Thus the reverse transformation V_C-$C_{Si} \rightarrow V_{Si}$ should occur into the low-spin state.

In equilibrium (with a given Fermi level), V_{Si} and V_C-C_{Si} are in different charge states. Provided the temperature is sufficiently low and the transformation is a rare event, the charge state can equilibrate at the final position before the reverse process takes place. Only at extreme temperatures we expect this picture to break down. Consequently, energy barriers for different charge states should apply for the two processes. In p-type and compensated material the barrier for the transformation $V_{Si} \rightarrow V_C$-C_{Si} is with 1.9 eV (V_{Si}^{1+}) to 2.4 eV (V_{Si}^-) much lower than the barrier of the reverse transformation of 6.1 eV $[(V_C\text{-}C_{Si})^{2+},\ \mu_F < 1.24\ \text{eV}]$ to 3.5 eV $[(V_C\text{-}C_{Si})^0,\ \mu_F < 2.19\ \text{eV}]$. In n-type material (i.e., for $\mu_F > 2.19$) this situation is reversed, when $(V_C\text{-}C_{Si})^-$ becomes the ground state. Now the transformation of $(V_C\text{-}C_{Si})^-$ into V_{Si}^- has a higher probability than the opposite process $V_{Si}^{2-} \rightarrow (V_C\text{-}C_{Si})^{2-}$.

A comparison between the migration barriers of the silicon vacancy and the transformation barriers should tell whether the silicon vacancy is trapped as a V_C-C_{Si} complex or whether it freely migrates. In n-type material V_{Si}^{2-} is stable (i.e., for $\mu_F > 1.76$ eV). The migration barrier (2.4 eV) is slightly smaller than the transformation barrier (2.7 eV) to the metastable V_C-C_{Si} complex. For $\mu_F > 2.19$ eV $(V_C\text{-}C_{Si})^-$ returns by a reverse transformation (2.4 eV) via V_{Si}^- to V_{Si}^{2-} with an even higher probability. For μ_F between 1.79 eV and 2.19 eV $(V_C\text{-}C_{Si})^0$ is relevant. Even though the barrier of the transformation V_C-$C_{Si} \rightarrow V_{Si}$ (3.5 eV) is larger, the migration of V_{Si} is essentially not hindered as V_{Si}^{2-} is the ground state. Thus, in n-type material, the vacancy should freely migrate.

On the other hand, for a Fermi level below 1.7 eV the V_C-C_{Si} complex is the ground state. Before a migration of V_{Si} may take place, it has to be preceded by a transformation V_C-$C_{Si} \rightarrow V_{Si}$. This gives rise to an additional barrier. For a Fermi level below midgap this barrier becomes large, i.e., 4.1 eV for $(V_C\text{-}C_{Si})^+$ and 6.1 eV for $(V_C\text{-}C_{Si})^{2+}$. This additional barrier allows a migration of V_C-C_{Si} via V_{Si} only at elevated temperatures, when the transformation V_C-$C_{Si} \rightarrow V_{Si}$ is thermally activated. At low temperatures this migration is kinetically hindered.

Instead, another migration channel is opened: the V_C-C_{Si} complex can dissociate at the expense of the binding energy. However, using the migration barrier for V_C between 3.5 eV (V_C^0) to 5 eV (V_C^{2+}) plus the binding energy as an estimate for the dissociation barrier, we conclude that the dissociation and the reverse transformation have similar probabilities. In p-type and compensated material ($\mu_F < 1.71$ eV) the migration of silicon vacancies is suppressed for moderate temperatures.

C. Carbon-interstitials

Apparently, the energetically lowest sites are the most relevant ones for the migration of the carbon interstitials. As discussed in Sec. III, these are the two split interstitials $C_{sp\langle 100\rangle}$ and $C_{spSi\langle 100\rangle}$. The migration of the energetically more favorable $C_{sp\langle 100\rangle}$ interstitial may proceed by two alternative routes: (a) by nearest-neighbor hops between adjacent carbon and silicon lattice sites in the sequence $C_{sp\langle 100\rangle} \rightarrow C_{spSi\langle 100\rangle} \rightarrow C_{sp\langle 100\rangle}$ and (b) by second-neighbor hops of the interstitial between neighboring carbon lattice sites.

We illustrate the migration event by nearest-neighbor hops in Fig. 10. Taking $C_{sp\langle 100\rangle}$ [Fig. 10(a)] as the initial configuration, the final configuration is $C_{spSi\langle 100\rangle}$ [Fig. 10(c)], which is located at the nearest neighbor silicon site. The saddle-point search yields the transition state shown in Fig. 10(b). The migration proceeds by a concerted motion of the dumbbell, such that one carbon atom approaches the neighboring silicon atom while the other returns into the position on the lattice. At the same time, the silicon neighbor moves out of this site to give room for a new carbon-silicon dumbbell. We have conducted a saddle-point search in the charge states 2^+, 1^+, neutral, and 1^- using a 64-atom cell and a special k point set. For the hop from $C_{sp\langle 100\rangle}$ to $C_{spSi\langle 100\rangle}$ we find a barrier of 1.7 eV and 0.9 eV for the charge states 2^+ and 1^+. The barriers of the second hop from $C_{spSi\langle 100\rangle}$ to $C_{sp\langle 100\rangle}$ amount to 0.7 eV and 0.2 eV, respectively, and are lower than those of the first hop. In the neutral and negative charge states the hop starts from the tilted configuration. The path is as discussed above. The barriers amount to 0.5 eV and 0.2 eV for $C_{sp\langle 100\rangle}^0$. Similar barriers are found in the case of $C_{sp\langle 100\rangle}^-$.

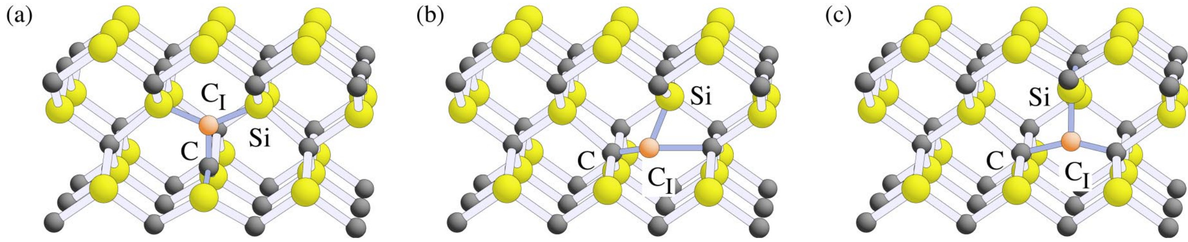

FIG. 10. Migration of carbon interstitials: (a) initial interstitial $C_{sp\langle 100\rangle}$, (b) transition state, (c) final interstitial $C_{spSi\langle 100\rangle}$

The migration of $C_{sp\langle 100\rangle}$ by second-neighbor hops can proceed in several different ways. Each of the carbon atoms of the dumbbell is surrounded by six neighboring carbon lattice sites. While one atom migrates to one of the neighboring carbon sites, the other moves back onto the lattice. We have investigated the hop of the (001)-oriented split interstitial in the (110) direction. The migration proceeds in a similar manner as the nearest-neighbor hop, except that now the destination is the adjacent carbon lattice site. The migration barriers we obtained with the saddle point search are listed in Table IV. They are comparable to the nearest-neighbor hop. Only for $C^{2+}_{sp\langle 100\rangle}$ we find a lower barrier for the second-nearest-neighbor hop (1.4 eV) than for the nearest-neighbor hop (1.7 eV).

The relatively small migration barrier contrasts the much larger energy difference found between the split interstitials and the tetrahedrally coordinated sites. As discussed in Sec. III B, at these sites carbon bonds are established at high-energy costs. Consequently, a relevant migration of carbon interstitials via these sites is unlikely.

The hexagonal interstitial is 1.4 eV (C^{2+}_{hex}) and 1.6 eV (C^{+}_{hex}) higher in energy than $C_{spSi\langle 100\rangle}$. This energy difference is only slightly lower than the migration barrier for $C^{2+}_{spSi\langle 100\rangle}$ and even higher in the case of $C^{1+}_{spSi\langle 100\rangle}$. Therefore we expect a higher-energy barrier for a migration via the hexagonal sites, particularly as the mechanism should initially proceed similar to the migration via split interstitial sites to avoid extensive bond breaking.

D. Silicon-interstitials

In Sec. III A we have shown that the two most favorable interstitial configurations are the tetrahedrally carbon-coordinated site and the (110)-oriented split interstitial. The first configuration is favored in *p*-type material and the latter is clearly dominating in *n*-type material. The migration between the energetically lowest sites may involve the other configuration as an intermediate site or may proceed by direct hops. As discussed previously, we assume that the charge state is not altered during a hop. Only in the intermediate configurations a charge transfer is allowed.

TABLE IV. Migration of carbon interstitials: Migration barriers E_m in eV for nearest-neighbor hops $C_{sp\langle 100\rangle}\leftrightarrow C_{spSi\langle 100\rangle}$ and second-neighbor hops. The migration of $C^0_{sp\langle 100\rangle}$ and $C^-_{sp\langle 100\rangle}$ starts from the tilted configuration.

	2^+	1^+	0	1^-
$C_{sp\langle 100\rangle}\rightarrow C_{spSi\langle 100\rangle}$	1.7	0.9	0.5	0.7
$C_{spSi\langle 100\rangle}\rightarrow C_{sp\langle 100\rangle}$	0.9	0.2	0.2	0.1
$C_{sp\langle 100\rangle}\leftrightarrow C_{sp\langle 100\rangle}$	1.4	0.9	0.5	0.6

In *p*-type material all migration paths begin and end at the Si_{TC} site. Two different types of migration mechanisms are discussed here and depicted in Fig. 11: (a) a kick-out mechanism that proceeds via the split interstitials $Si_{sp\langle 100\rangle}$ and $Si_{sp\langle 110\rangle}$ as intermediate sites and (b) a direct migration between the tetrahedral interstitial sites Si_{TC} and Si_{TSi}. The kick-out mechanism consists of two steps. In the first step the tetrahedral interstitial moves towards a silicon neighbor and kicks it out of its lattice site. A split interstitial is formed as an intermediate site. Next, the second atom proceeds towards the closest tetrahedral interstitial site. We have determined the migration paths and the energy barriers for the two processes by a saddle-point search using a 64-atom cell and special *k* points ($2\times2\times2$ Monkhorst-Pack mesh). While the path via the $Si_{sp\langle 100\rangle}$-configuration proceeds entirely along the (100) direction, the path via the $Si_{sp\langle 110\rangle}$ interstitial is curved. The transition state in both cases lies close to the split interstitial configuration. The energy barriers for the kick-out and the kick-in process are listed in Table V. The kick-out barrier via the $Si_{sp\langle 100\rangle}$ interstitials amounts to 3.5 eV and is only 0.1 eV higher than the barrier obtained via the $Si_{sp\langle 110\rangle}$ interstitial. The results show that the two intermediate interstitial configurations are not very stable as the barriers for the second event amount to 0.03 eV and 0.05 eV, respectively. We expect that the interstitial passes through the intermediate site without any significant delay. Therefore a charge transfer that could convert the $Si_{sp\langle 110\rangle}$ interstitial from the transient 4^+-state into 2^+ or 1^+ (the ground state in *p*-type material) seems unlikely.

The migration between the tetrahedral interstitial sites Si_{TC} and Si_{TSi} proceeds directly through the interstice. The migration path passes through the hexagonal configurations along the axis connecting the initial and final configurations. The transition state lies close to the ideal position of the hexagonal site. The saddle-point search yields an energy barrier of 3.5 eV for the hop $Si_{TC}\rightarrow Si_{TSi}$. For the hop $Si_{TSi}\rightarrow Si_{TC}$ we obtain a barrier of 0.3 eV.

Since for Si_{TSi} the charge state 4^+ is not the ground state, a charge transfer can change it with some probability. Then the interstitial could alternatively migrate via the split interstitial $Si^{2+}_{sp\langle 110\rangle}$ with a low barrier (cf. Table V). However, this route is not very likely. Instead the Si^{2+}_{TSi} (or Si^{3+}_{TSi}) would move to the Si_{TC} site with an even lower barrier.

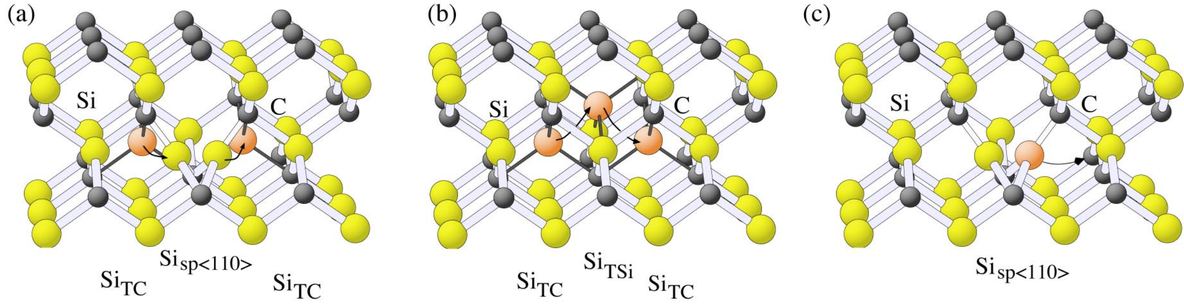

FIG. 11. Migration of silicon interstitials: (a) kick-out migration of Si_{TC} via the split interstitial $Si_{sp\langle 110\rangle}$, (b) migration via the tetrahedral interstitial sites Si_{TC} and Si_{TSi}, and (c) jumps between adjacent $Si_{sp\langle 110\rangle}$ configurations.

In compensated and n-type material, we consider the kick-out migration via the split interstitials $Si^0_{sp\langle 110\rangle}$. As one of the silicon atoms of $Si_{sp\langle 110\rangle}$ hops towards the next silicon site it kicks out the silicon atom at this site in the corresponding (110) direction to form a new split interstitial. For this process we find a migration barrier of 1.4 eV. For the positive split interstitial we obtain a barrier of 1.0 eV. The orientation of the split interstitial can change by a rotation around the $\langle 100\rangle$ axis. For example, the rotation around the (001)-axis changes the orientation from (110) to $(1\bar{1}0)$. It is associated with an energy barrier of 1.3 eV ($Si^0_{sp\langle 110\rangle}$).

In order to understand whether the kick-out migration via $Si^0_{sp\langle 110\rangle}$ is the dominating mechanism, we have to compare its activation energy with that of other possible mechanisms at intrinsic and n-type doping conditions. In comparison to a migration via the interstitial Si^{2+}_{TSi}, we find that this configuration for μ_F above 1.3 eV already lies higher in energy than the saddle point of $Si_{sp\langle 110\rangle}$. Furthermore, according to our estimates also Si_{TC} and $Si_{sp\langle 100\rangle}$ should be correspondingly higher in energy for a Fermi level close to the conduction band. Thus we conclude that the dominating mechanism under intrinsic and n-type conditions is the migration via the $Si_{sp\langle 110\rangle}$ interstitial.

TABLE V. Migration of silicon interstitials: Migration barriers E_m in eV for different migration paths. The migration paths are shown in Fig. 11. The charge state is 4^+ unless indicated otherwise. See text for details.

	TC↔ sp⟨100⟩	TC↔ sp⟨110⟩	TC↔TSi
1→2	3.5	3.4	3.5
2→1	0.03	0.05	0.3
	sp⟨110⟩ (+) ↔ sp⟨110⟩	sp⟨110⟩ (0) ↔ sp⟨110⟩	sp⟨110⟩ (0) ↔ sp⟨1$\bar{1}$0⟩
1↔2	1.0	1.4	1.3
	TSi (2+) ↔ sp⟨100⟩	TSi (3+) →TC	TSi (2+) →TC
1→2	0.1	0.04	0.03
2→1	0.25		

VI. DISCUSSION

Our analysis of the mobile intrinsic point defects in Secs. III and IV and their migration mechanisms in Sec. V reveals a complex dependence of the abundance and the migration on the doping conditions. In the following we discuss the implications of our findings for the self-diffusion and dopant diffusion. The mechanisms that enter the discussion are summarized schematically in Fig. 1 and the associated energy barriers are listed in Tables III–V. This microscopic picture of the point defect migration has also implications for the annealing mechanism of vacancies. This aspect is treated, together with an analysis of Frenkel pairs, in a separate paper.[23]

A. Self diffusion

The self-diffusion constants of carbon and silicon, D_C and D_{Si}, are given by the sum of different diffusion mechanisms, in particular of mechanisms based on vacancy and interstitial migration. For instance, the carbon self-diffusion constant is given by

$$D_C = \sum_i D_i^{V_C} + \sum_j D_j^{I,C} + \cdots, \tag{8}$$

where $D_i^{V_C}$ and $D_j^{I,C}$ are the diffusion constants of vacancy and interstitial mechanisms, respectively, and i, j denote the different migrations paths of the mobile defect in a specific charge state. Each contribution is proportional to the concentration of the mobile defect c_i [cf. Eq. (1)] and its diffusivity d_i, as given by the formation energy E_i^f and the migration energy barrier E_i^m, respectively,

$$D_i = D_i^0 \exp\left(- \frac{E_i^f(\Delta\mu, \mu_F) + E_i^m}{k_B T} \right), \tag{9}$$

where D_i^0 is a constant prefactor that is determined by geometrical and entropy factors. The activation energy $Q_i = E_i^f(\Delta\mu,\mu_F) + E_i^m$ that determines the exponential factor essentially characterizes the contribution of each migration mechanism. The factor may vary over several orders of magnitude for different mechanisms, whereas the prefactors D_i^0 typically have a similar order of magnitude. Thus a comparison of the activation energies of different diffusion mecha-

TABLE VI. Activation energy for the self-diffusion as mediated by vacancies and interstitials (cf. text for details).

Carbon self-diffusion					Silicon self-diffusion				
Defect	$Q(\mu_f,\Delta\mu)$ (eV)			μ_F (eV)	Defect	$Q(\mu_f,\Delta\mu)$ (eV)			μ_F (eV)
	Explicit	Si-rich	C-rich	Range		Explicit	Si-rich	C-rich	Range
V_C^{2+}	6.6 eV $+2\mu_F$ $-\Delta\mu$	6.6–9.0	7.2–9.6	0.0–1.2	V_{Si}^{1-}	12.2 eV $-\mu_F$ $+\Delta\mu$	11.6–10.4	11.0–9.8	0.6–1.8
V_C^0	7.3 eV $-\Delta\mu$	7.3	7.9	1.2–E_C	V_{Si}^{2-}	13.1 eV $-2\mu_F$ $+\Delta\mu$	9.6–7.7	9.0–7.1	1.8–E_C
$C_{sp\langle 100\rangle}^{2+}$	6.7 eV $+2\mu_F$ $+\Delta\mu$	6.7–7.8	6.1–7.2	0.0–0.6	Si_{TC}^{4+}	7.8 eV $+4\mu_F$ $-\Delta\mu$	7.8–12.6	8.4–13.2	0.0–1.2
$C_{sp\langle 100\rangle}^{1+}$	6.6 eV $+\mu_F$ $+\Delta\mu$	7.2–7.9	6.6–7.3	0.6–0.8		7.7 eV $+4\mu_F$ $-\Delta\mu$	7.7–12.5	8.3–13.1	0.0–1.2
$C_{sp\langle 100\rangle}^{0}$	7.7 eV $+\Delta\mu$	7.2	6.6	0.8–1.8	$Si_{sp\langle 110\rangle}^{0}$	9.9 eV $-\Delta\mu$	9.9	10.5	1.1–E_C
$C_{sp\langle 100\rangle}^{-}$	9.1 eV $-\mu_F$ $+\Delta\mu$	7.3–6.7	6.7–6.1	1.8–E_C					
Expt.[a] 3C	8.72 eV$\pm$0.14 eV			Undoped	Exp.[a] 3C	9.45 eV$\pm$0.05 eV			undoped
Expt.[b] 4H	7.14 eV$\pm$0.05 eV			Intrinsic	Exp.[b] 4H	7.22 eV$\pm$0.07 eV			intrinsic
Expt.[b] 4H	8.20 eV$\pm$0.08 eV			n-type	Exp.[b] 4H	8.18 eV$\pm$0.10 eV			n-type

[a]References 7 and 8: experiments on polycrystalline 3C-SiC samples.
[b]References 9 and 10: experiments on 4H-SiC single crystals.

nisms reveals the dominant contribution to self-diffusion for different doping and growth conditions that enter Q via $\Delta\mu$ and μ_F. In Table VI the activation energies for vacancy- and interstitial-mediated self-diffusion are listed. Q is given as an explicit function of μ_F and $\Delta\mu$. At Si-rich conditions $\Delta\mu$ is 0 and assumes a value of $-H_f^{SiC}$ (-0.61 eV in the present calculations) at C-rich conditions. For the charged defects the range of μ_F is given in which the particular charge state is stable. The variation of Q with the Fermi level can be substantial, i.e., for Si_{TC}^{4+} it amounts up to 5 eV. For a typical diffusion temperature of 1000 K the change of $\Delta Q\sim 1$ eV translates into a variation of the diffusion constant over five orders of magnitude. This striking dependence on the doping conditions is known as the Fermi level effect.[54] Table VI also includes the activation energies deduced from recent self diffusion experiments for polycrystalline[7,8] 3C-SiC and for 4H-SiC single crystals.[9,10] To the best of our knowledge, these are the first experiments that quantitatively analyzed the self-diffusion constant. A radiotracer diffusion technique was used to obtain the diffusion profiles.

For the carbon self-diffusion our results show a similar importance of the vacancy-mediated and interstitial-based self-diffusion in Si-rich material. There is no clear dominance of either mechanism. In C-rich material, on the other hand, the split interstitial mediated self-diffusion dominates for all doping conditions. Since in compensated and n-type material the split interstitial and the vacancy are neutral, the Fermi level effect is absent. Only in p-type material a variation of the activation energy about 1 eV is present.

The silicon self-diffusion in p-type and compensated material is mainly dominated by the silicon interstitials. In p-type material the migration is mediated by the tetrahedral carbon-coordinated interstitial Si_{TC}, both, under Si-rich and C-rich conditions. Here the metastability of the silicon vacancy suppresses its participation in the self diffusion. In Si-rich compensated material the silicon split interstitial $Si_{sp\langle 110\rangle}$ is relevant. Only in n-type, Si-rich material a dominant contribution of the silicon vacancy V_{Si} should be observed. The larger abundance of silicon vacancies under C-rich conditions leads to its dominance already in compensated material. The variation of the activation energy of the silicon self-diffusion is more pronounced than for the carbon self-diffusion. A Fermi level effect is predicted under p-type and n-type conditions. The variations amount to 2 eV, both, in C-rich and Si-rich materials.

Experimentally the silicon and carbon self-diffusion was investigated in nominally undoped polycrystalline 3C-SiC.[7,8] For the carbon self-diffusion an activation energy of 8.72 eV was obtained. The observed silicon self-diffusion was described[8] by an activation energy of 9.45 eV. From the description of the experiments it is not obvious whether they were carried out in C-rich or Si-rich conditions. Therefore we compare the experimental results with our values for C-rich and Si-rich conditions for an intrinsic Fermi level. For the carbon self-diffusion we obtain an activation energy of 7.3 eV (V_C^0, Si rich) and 6.6 eV ($C_{sp\langle 110\rangle}$, C rich), respectively. The experimental value exceeds our theoretical results by 1.4 eV–2.0 eV. This discrepancy cannot be explained in terms of the missing information about $\Delta\mu$ or a variation of μ_F. Our results indicate a value of at most 8 eV. Only if the interstitial diffusion was completely suppressed during the experiment and the sample was rather p type than intrinsic, the activation energy could be explained by that of V_C^{2+}. Here the polycrystalline nature of the material may also affect the defect equilibrium, i.e., the grain boundaries may act as sinks for interstitials. For the silicon self-diffusion we obtain an activation energy of 9.9 eV ($Si_{sp\langle 110\rangle}$, Si rich) and 10.4 eV ($V_{Si}^-$, C rich) in intrinsic material. In this case the experimental value is in good agreement with our results.

Even though our investigation of the defect migration was conducted for 3C-SiC, we expect that our results may provide a first insight into the diffusion processes in other polytypes. This expectation is supported by the finding[19,24,25] of comparable energetics and bonding of vacancies in 3C-SiC and 4H-SiC. For example, similar transformation barriers are found for the neutral silicon vacancy in 3C-SiC (this work) and 4H-SiC.[21] The main difference is the larger energy gap in 4H-SiC. Intrinsic conditions, thus, apply in 4H-SiC to $\mu_F\sim 1.7$ eV. A comparison of our results with the

activation energy of the carbon self-diffusion in 4*H*-SiC single crystals shows a much better agreement than for the polycrystalline 3*C*-SiC. However, for the silicon self-diffusion our prediction of about 9 eV substantially deviates from the experimental result of 7.2 eV, unless we place the Fermi level above midgap at around 2.3 eV. *n*-type 4*H*-SiC is not covered by our results, since the relevant charge states of the vacancies and interstitials in 4*H*-SiC are not present in 3*C*-SiC.

In light of our expectation the large variation of the experimental activation energies between 3*C*-SiC and 4*H*-SiC is surprising. Besides the polycrystalline nature of the cubic material, an incomplete point defect equilibrium or the preferential injection of either vacancies or interstitials at the interface of the tracer material and SiC may be responsible. Here we note that the investigation of the aluminum and boron diffusion[4,5] indicates a slower silicon self-diffusion than observed in the tracer diffusion experiments. This finding inevitably affects the given prefactor and activation energies.

B. Dopant migration

In SiC, dopant atoms may substitute for carbon or silicon. For example, aluminum and phosphorus are known to preferentially bind to the silicon sublattice[55] and nitrogen prefers carbon sites.[55] Boron is predicted to bind either to the carbon or silicon sublattice[56,57] depending on the stoichiometry of the sample (C/Si ratio). The migration of these dopants is mediated by mobile intrinsic defects. A mobile vacancy and a substitutional dopant atom may form a mobile dopant-vacancy complex. An attractive interaction within the mobile pair enables migration until the pair eventually dissociates. Mobile interstitials may initiate a migration of the dopant by a kick-out reaction.

In equilibrium, the dominating mechanism of dopant diffusion depends not only on the involved migration barriers but also on the abundance of the involved intrinsic defects. A transient enhanced dopant diffusion that was recently observed for boron[1,2] and aluminum[3] is triggered by an excess concentration of intrinsic defects, generated for example by the dopant implantation. Assuming that a similar amount of interstitials and vacancies is generated, the migration barriers for different mechanisms are the relevant quantities to compare. Naturally, for dopants on the carbon and the silicon sublattice different migration mechanisms apply. Even though the migration mechanism should certainly be dopant dependent, some general conclusions about the dopant diffusion can be drawn from our results for the diffusion of vacancies and interstitials.

First of all, the availability of the mobile defects depends on the doping conditions. The discussion in Sec. IV showed that a mechanism based on silicon vacancies is not available in *p*-type material. The metastability of V_{Si} in *p*-type material should affect dopant complexes with a silicon vacancy in a similar way. Thus only the migration of a donor complex that involves the carbon vacancy should be relevant. In such a complex the dopant and the vacancy may be nearest neighbors or second-nearest neighbors, when the dopant substitutes for silicon or carbon, respectively. Whereas the migration of the second-neighbor pair proceeds entirely on the carbon sublattice by second-neighbor hops, the migration of the nearest-neighbor pair involves an initial exchange of the dopant and the vacancy and further migration of the vacancy around the dopant.[58] This may only be accomplished by second neighbor hops. A mechanism based on nearest-neighbor hops fails as the necessary V_{Si}-Si_C complexes are unstable. In *n*-type material a mechanism based on silicon vacancies becomes available. With the same arguments as above a migration will involve only second-neighbor hops of the vacancy.

Consequently, the diffusion of acceptors on the silicon sublattice most likely is mediated by silicon interstitials in *p*-type material. More general conclusions on the role of the mechanisms based on carbon and silicon interstitials are not possible. Here we only note that carbon interstitials and silicon interstitials (in compensated and *n*-type material) have lower migration barriers than the corresponding vacancies. The interstitial-mediated dopant migration may be limited by the availability of interstitials and the barriers associated with the migration of the dopant interstitial.

These arguments are supported by our findings for boron[57] and by recent experiments on the diffusion of boron[1,2,4,5] and aluminum.[4] Our calculations reveal that a migration via the nearest-neighbor complex B_{Si}-V_C is unlikely. The barrier of the initial transformation has a similar magnitude as the transformation of V_C-C_{Si} into V_{Si} in *p*-type material. Furthermore, the nearest-neighbor complex B_{Si}-V_C is practically unstable in *p*-type material. The migration of the second-neighbor complex B_C-V_C consists of three hops and involves migration barriers in *p*-type material of as much as 5.6 eV, which exceeds the barrier for the carbon vacancy. We find much lower migration barriers for a kick-out mechanism by silicon interstitials (B_{Si}) or carbon interstitials (B_C) and a subsequent migration of the boron-interstitials. Though earlier experiments[6] favored a vacancy-related mechanism, the recent quantitative modeling of boron diffusion experiments[2,4,5] attributes the diffusion to a kick-out mechanism based on silicon interstitials. A similar conclusion was suggested by coimplantation experiments.[1] Here the transient enhanced diffusion observed after boron implantation was suppressed by carbon coimplantation and elevated by silicon coimplantation.

VII. SUMMARY AND CONCLUSION

A picture of the defect migration has been derived from theoretical investigations based on an *ab initio* method within the framework of DFT. The analysis of the microscopic structure, the abundance, and the migration mechanisms of interstitials and vacancies contribute to this picture. A strong influence of the doping conditions is reported for the mobile silicon defects. Among the silicon interstitials two different interstitial configurations are relevant, the tetrahedrally carbon-coordinated interstitial in *p*-type material and the split interstitial in compensated and *n*-type material. This affects the interstitial migration in *p*-type material: the migration of the tetrahedrally carbon-coordinated interstitial is

slower than the migration of the split interstitial. A metastability of the silicon vacancy occurs in *p*-type and compensated material. It transforms into the more stable carbon vacancy-antisite complex. This transformation of the silicon vacancy is more likely than its migration. The thermal activation of the reverse process determines the mobility of the vacancy-antisite complex. A central result is the finding that interstitials are more mobile than vacancies.

The importance of interstitials and vacancies in the self-diffusion and dopant diffusion is determined by their abundance and diffusivity. The discussion of the two factors showed that the interstitials play a significant role in the self-diffusion. For instance, silicon interstitials dominate the silicon self-diffusion in *p*-type material. The dominance of carbon interstitials in the carbon self-diffusion stems from an overcompensation of their relatively low abundance by their higher mobility. For the dopant diffusion, similar qualitative conclusions are drawn and outlined for the case of boron, for which theoretical calculations indicate an important role of the interstitial-mediated diffusion.

ACKNOWLEDGMENTS

We acknowledge fruitful discussions with Dr. G. Pensl, who also initiated this project. This work was supported by the Deutsche Forschungsgemeinschaft, SFB 292 and SiC Research Group.

*Electronic address: bockstedte@physik.uni-erlangen.de

[1] M. Laube, G. Pensl, and H. Itoh, Appl. Phys. Lett. **74**, 2292 (1999).

[2] M.S. Janson, M.K. Linnarsson, A. Hallén, B.G. Svensson, N. Nordell, and H. Bleichner, Appl. Phys. Lett. **76**, 1434 (2000).

[3] I.O. Usov, A.A. Suvorova, V.V. Sokolov, Y.A. Kudryavtsev, and A.V. Suvorov, J. Appl. Phys. **86**, 6039 (1999).

[4] A.O. Konstantinov, Sov. Phys. Semicond. **26**, 151 (1992).

[5] H. Bracht, N.A. Stolwijk, M. Laube, and G. Pensl, Appl. Phys. Lett. **77**, 3188 (2000).

[6] E.N. Mokhov, E.E. Goncharov, and G.G. Ryabova, Sov. Phys. Semicond. **18**, 27 (1984).

[7] J.D. Hong, M.D. Hon, and R.F. Davis, Ceram. Int. **5**, 155 (1979).

[8] M.H. Hon, R.F. Davis, and D.E. Newbury, J. Mater. Sci. **15**, 2073 (1980).

[9] J.D. Hong and R.F. Davis, J. Am. Ceram. Soc. **63**, 546 (1980).

[10] J.D. Hong, R.F. Davis, and D.E. Newbury, J. Mater. Sci. **16**, 2485 (1981).

[11] A. Kawasuso, H. Itoh, S. Okada, and H. Okumura, J. Appl. Phys. **80**, 5639 (1996).

[12] G. Brauer, W. Anwand, P.G. Coleman, A.P. Knights, F. Plazaola, Y. Pacaud, W. Skorupa, J. Störmer, and P. Willutzki, Phys. Rev. B **54**, 3084 (1996).

[13] A. Polity, S. Huth, and M. Lausmann, Phys. Rev. B **59**, 10 603 (1999).

[14] A. Kawasuso, F. Redmann, R. Krause-Rehberg, T. Frank, M. Weidner, G. Pensl, P. Sperr, and H. Itoh, J. Appl. Phys. **90**, 3377 (2001).

[15] H. Itoh, A. Kawasuso, T. Ohshima, M. Yoshikawa, I. Nashiyama, S. Tanigawa, S. Misawa, H. Okumura, and S. Yoshida, Phys. Status Solidi A **162**, 137 (1997).

[16] T. Wimbauer, B.K. Meyer, A. Hofstaetter, A. Scharmann, and H. Overhof, Phys. Rev. B **56**, 7384 (1997).

[17] H.J. von Bardeleben, J.L. Cantin, L. Henry, and M.F. Barthe, Phys. Rev. B **62**, 10 841 (2000).

[18] N.T. Son, P.N. Hai, and E. Janzén, Phys. Rev. B **63**, 201201 (2001).

[19] M. Bockstedte, M. Heid, A. Mattausch, and O. Pankratov, Mater. Sci. Forum **389–393**, 471 (2002); Phys. Rev. B **67**, 193102 (2003).

[20] T. Lingner, S. Greulich-Weber, J.-M. Spaeth, U. Gerstmann, E. Rauls, Z. Hajnal, Th. Frauenheim, and H. Overhof, Phys. Rev. B **64**, 245212 (2001).

[21] E. Rauls, Th. Lingner, Z. Hajnal, S. Greulich-Weber, Th. Frauenheim, and J.-M. Spaeth, Phys. Status Solidi B **217**, R1 (2000).

[22] M. Bockstedte and O. Pankratov, Mater. Sci. Forum **338–342**, 949 (2000).

[23] M. Bockstedte, A. Mattausch, and O. Pankratov (unpublished).

[24] A. Zywietz, J. Furthmüller, and F. Bechstedt, Phys. Rev. B **59**, 15 166 (1999).

[25] L. Torpo, M. Marlo, T.E.M. Staab, and R.M. Nieminen, J. Phys.: Condens. Matter **13**, 6203 (2001).

[26] M. Bockstedte, A. Kley, J. Neugebauer, and M. Scheffler, Comput. Phys. Commun. **200**, 107 (1997).

[27] P. Hohenberg and W. Kohn, Phys. Rev. **136**, B864 (1964).

[28] W. Kohn and J.L. Sham, Phys. Rev. **140**, A1133 (1965).

[29] J.P. Perdew and A. Zunger, Phys. Rev. B **23**, 5048 (1981).

[30] G. Makov, R. Shah, and M.C. Payne, Phys. Rev. B **53**, 15 513 (1996).

[31] H.J. Monkhorst and J.D. Pack, Phys. Rev. B **13**, 5188 (1976).

[32] G. Makov and M.C. Payne, Phys. Rev. B **51**, 4014 (1995).

[33] J. Lento, J.-L. Mozos, and R.M. Nieminen, J. Phys.: Condens. Matter **14**, 2637 (2002).

[34] N. Troullier and J.L. Martins, Phys. Rev. B **43**, 1993 (1991).

[35] P. Blöchl, E. Smargiassi, R. Car, D.B. Laks, W. Andrioni, and S.T. Pantelides, Phys. Rev. Lett. **70**, 2435 (1993).

[36] M. Bockstedte and M. Scheffler, Z. Phys. Chem. (Munich) **200**, 195 (1997).

[37] S.B. Zhang and J.E. Northrup, Phys. Rev. Lett. **67**, 2339 (1991).

[38] U. Scherz and M. Scheffler, in *Semiconductors and Semimetals*, edited by Willardson and Beer (Academic Press, New York, 1993), Vol. 38, Chap. 1.

[39] P.W. Anderson, Phys. Rev. B **34**, 953 (1975).

[40] G.A. Baraff, E.O. Kane, and M. Schlüter, Phys. Rev. Lett. **43**, 956 (1979).

[41] E. Pehlke and P. Kratzer (private communication).

[42] I.V. Ionova and E.A. Carter, J. Chem. Phys. **98**, 6377 (1993).

[43] A. Mattausch, M. Bockstedte, and O. Pankratov (unpublished).

[44] L. Torpo, S. Pöykkö, and R.M. Nieminen, Phys. Rev. B **57**, 6243 (1998).

[45] P. Deák, J. Miró, A. Gali, L. Udvardi, and H. Overhof, Appl. Phys. Lett. **75**, 2103 (1999).

[46] A. Zywietz, J. Furthmüller, and F. Bechstedt, Phys. Rev. B **61**, 13 655 (2000).

[47] A. Zywietz, J. Furthmüller, and F. Bechstedt, Phys. Rev. B **62**, 6854 (2000).

[48] L. Torpo and R.M. Nieminen, Appl. Phys. Lett. **74**, 221 (1999).
[49] A. Mattausch, M. Bockstedte, and O. Pankratov, Mater. Sci. Forum **353–356**, 323 (2001).
[50] B. Chen, Q.-M. Zhang, and J. Bernholc, Phys. Rev. B **49**, 2985 (1994).
[51] J. Dabrowski and J.E. Northrup, Phys. Rev. B **49**, 14 286 (1994).
[52] J.A. Van Vechten, J. Phys. C **17**, L933 (1984).
[53] W.A. Harrison, Phys. Rev. B **57**, 9727 (1998).
[54] T.Y. Tan and U. Goesele, J. Appl. Phys. **61**, 1841 (1987).
[55] S. Greulich-Weber, Phys. Status Solidi A **162**, 95 (1997).
[56] A. Fukumoto, Phys. Rev. B **53**, 4458 (1996).
[57] M. Bockstedte, A. Mattausch, and O. Pankratov, Mater. Sci. Forum **353–356**, 447 (2001).
[58] O. Pankratov, H. Huang, T. Diaz dela Rubia, and C. Mailhiot, Phys. Rev. B **56**, 13 172 (1997).